

# Towards reliable calcification detection: calibration of uncertainty in object detection from coronary optical coherence tomography images

Hongshan Liu<sup>a</sup>, Xueshen Li<sup>a</sup>, Abdul Latif Bamba<sup>b</sup>, Xiaoyu Song<sup>c</sup>, Brigitta C. Brott<sup>d</sup>, Silvio H. Litovsky<sup>d</sup>, Yu Gan<sup>a,\*</sup>

<sup>a</sup>Stevens Institute of Technology, Biomedical Engineering, Hoboken, NJ, 07030

<sup>b</sup>Columbia University, Department of Electrical Engineering, New York, NY, 10027

<sup>c</sup>The Icahn School of Medicine at Mount Sinai, New York, NY, 10029

<sup>d</sup>The University of Alabama at Birmingham, School of Medicine, Birmingham, AL, 35487

## Abstract.

**Significance:** Optical coherence tomography (OCT) has become increasingly essential in assisting the treatment of coronary artery disease (CAD). However, unidentified calcified regions within a narrowed artery could impair the outcome of the treatment. Fast and objective identification is paramount to automatically procure accurate readings on calcifications within the artery.

**Aim:** We aim to rapidly identify calcification in coronary OCT images using a bounding box and reduce the bias of predicting in automated prediction models.

**Approach:** We first adopt a deep learning-based object detection model to rapidly draw the calcified region from coronary OCT images using bounding box. We measure the uncertainty of predictions based on the expected calibration errors, thus assessing the certainty level of detection results. To calibrate confidence scores of predictions, we implement dependent logistic calibration using each detection result's confidence and center coordinates.

**Results:** We have developed an object detection module to draw the boundary of calcified region at a rate of 140 frame per second. With the calibrated confidence score of each prediction, we lower the uncertainty of predictions in calcification detection and eliminate the estimation bias from various object detection methods. The calibrated confidence of prediction results in a confidence error of approximately 0.13, suggesting that the confidence calibration on calcification detection could provide a more trustworthy result.

**Conclusions:** Given the rapid detection and effective calibration of the proposed work, we expect it can assist clinical evaluation of treating the CAD during the imaging-guided procedure.

**Keywords:** Optical Coherence Tomography, Coronary Artery Disease, Deep Learning, Calibration.

\*Yu Gan, [ygan5@stevens.edu](mailto:ygan5@stevens.edu)

## 1 Introduction

Optical coherence tomography (OCT) can acquire high-resolution cross-sectional images of coronary arteries. The high quality and detailed information from coronary OCT images facilitates the treatment of coronary artery diseases (CAD). Coronary artery disease causes 1 of every 5 deaths in Europe<sup>1</sup> and 1 of every 6 deaths in the US,<sup>2</sup> and remains one of the leading causes of morbidity and mortality in developed countries.<sup>3</sup> Coronary atherosclerosis is caused by the gradual buildup of plaque resulting from the depositing of calcium, lipids, and macrophages from the luminal blood

into the arterial intima. Coronary atherosclerosis compounds and augments the risks of heart attack and heart failure. When treated improperly or left unattended, coronary atherosclerosis blocks the pathways to the heart's main arteries, known as the coronary arteries. Potential effects of plaque in CAD include chest pain, shortness of breath, heart failure, myocardial infarction, and sudden death.

A typical treatment for CAD is percutaneous coronary intervention (PCI), which is a non-surgical procedure used to treat the narrowing of the heart's coronary arteries. Unidentified calcified tissues within a narrowing artery often negatively impact the benefits of treatment. Approximately 700,000 PCI are performed every year in the US, and calcifications have been found in 17% to 35% of patients undergoing the procedure,<sup>4-6</sup> highlighting a need to precisely locate the existence and extent of calcifications. Most PCI procedures involve using stents to open up obstructed coronary arteries.<sup>7</sup> During the PCI procedure, a catheter with a tiny, folded balloon on its tip is inserted into the blood vessels until it arrives at the site where the plaque buildup is causing a blockage. At that point, the balloon is inflated to compress the plaque against the artery walls, therefore widening the passageway, and restoring blood flow to the heart. After that, the balloon is deflated and removed. A stent implantation is performed in the plaque buildup area to keep the artery open after removing the balloon.<sup>8</sup> Excess coronary calcification is highly related to the sub-optimal deployment of the stent in the coronary during the PCI.<sup>9</sup> Major calcifications are of great concern for two reasons.<sup>10</sup> Calcifications can lead to stent underexpansion and strut malapposition. Malapposition of stent struts (e.g. an empty space between the strut and the adjacent vessel wall) might preclude healthy endothelial tissue growth. Even though stent deployment is generally effective in the short-term, stent efficacy can be reduced and the risk can be increased by adverse clinical events, such as in-stent restenosis and thrombosis in the medium- and long-term.<sup>11-17</sup>

Coronary imaging guidance during PCI is one of the key determinants of treatment outcomes. Imaging is integral to every stage of PCI, such as assessment of lesion severity, preprocedural planning, optimization, and management of immediate complications.<sup>18,19</sup> Optical coherence tomography has significant advantages for characterizing coronary calcification that typically has a signal-poor area with sharply delineated borders.<sup>20</sup> A typical OCT system can achieve a high axial resolution at the micron level and a penetration depth of up to 2 mm, indicating superior imaging capability.<sup>21,22</sup> Detection of calcified regions within coronary OCT images is critical for intervention.<sup>23</sup> On account of this, developing an object detection algorithm that is capable of detecting calcification in OCT images is essential.

Deep learning has been increasingly explored in analyzing the diseased tissue in coronary OCT images.<sup>24</sup> Existing research work<sup>25–30</sup> have conducted extensive studies to automatically identify plaque in coronary OCT images. A weighted majority voting from different Convolutional Neural Networks (CNN)<sup>26</sup> was used to solve the multi-class classification problem of pathological formations in coronary artery tissues. A deep convolutional architecture named SegNet segmented calcification in coronary OCT images.<sup>10</sup> A two-step deep learning approach<sup>27</sup> characterizes plaques in coronary arteries in OCT images, by first localizing the major calcification lesions using the CNN model and second applying the deep learning model (SegNet) to provide pixel-wise classifications of calcified plaques. A modified deep convolutional segmentation model UNet<sup>28</sup> was used to identify calcification in coronary OCT images. The segmentation module in MASK-RCNN is employed to identify erosion region.<sup>31</sup> Currently, the most popular way to perform automated analysis on OCT images is deep learning-based segmentation, which makes the pixel-wise classification and outputs the detailed shape and location of tissue of interest. Demonstrably, segmentation architecture results in large computational costs due to burden from the pixel-wise classification. By

virtue of this, a more efficient way of enacting automated analysis of coronary images is through the use of object detection, which outputs the bounding box of tissue region rather than pixel-wise classification of tissue region, in order to efficiently identify the diseased region in coronary images.

While existing works also focus more on increasing the accuracy of deep learning models, the quality of predictions can be negatively impacted by overconfident deep learning models.<sup>32</sup> When an overconfident prediction is produced, the deep learning models tend to be excessively complex with respect to the structure of network. The overconfidence issue can lead to unreliable predictions that are biased by the specific network structure. In general, recalibration methods of the well-trained model, such as Platt scaling,<sup>33</sup> histogram binning,<sup>34</sup> temperature scaling,<sup>35</sup> can improve the calibration of the overconfident prediction results. Besides, model ensemble methods<sup>36,37</sup> can also reduce overconfidence by aggregating the prediction results over multiple models. However, there are limited studies on correcting overconfident predictions in coronary OCT images. In OCT-related CAD treatment, over-confidence could be dangerous, as confidence is often learned as the likelihood that the prediction is correct. Therefore, in safety-critical and risk-sensitive applications in clinical diagnosis, it is crucial to quantify and calibrate the uncertainty of predictions.

In this work, we aim to achieve reliable calcification detection for patients with CAD to boost the efficiency of clinical diagnosis. We summarize our contributions as:

1. We detect calcification in coronary OCT images via an object detection-based deep learning model. The object detection process delineates the bounding box of calcified region within OCT images, providing a computationally efficient solution in comparison with conventional segmentation methods.

2. We propose to calibrate the confidence of coronary object detection task. We use a dependent logistic calibration method to reduce the bias of uncertainty induced by the training of neural networks.
3. We quantitatively and qualitatively evaluate the effectiveness of the proposed work on a human coronary dataset. The experimental results demonstrate the accuracy and speed of calcification detection and also the effectiveness to reduce the bias of confidence among two most popular object detection methods.

## 2 Methods

The workflow is shown in Fig. 1. The steps are: (1) The coronary OCT data is first processed by a data augmentation module to create motion-blurred and horizontally flipped copies of each original OCT image. (2) The coronary OCT data after augmentation is trained by deep learning object detection models and outputs the detection results on test data. (3) Detections containing bounding box coordinates and confidence scores are processed through dependent logistic calibration and output a calibrated confidence score for each predicted bounding box.

### 2.1 Data collection

Samples are imaged by the spectral domain OCT system (Thorlabs Ganymede, Newton, NJ) with an axial resolution of  $3 \mu\text{m}$  and a lateral resolution of  $4 \mu\text{m}$  in air. Autopsy specimens of human heart vessels are collected and imaged through the same protocol in.<sup>38,39</sup> All images are acquired in the laboratory at the University of Alabama.

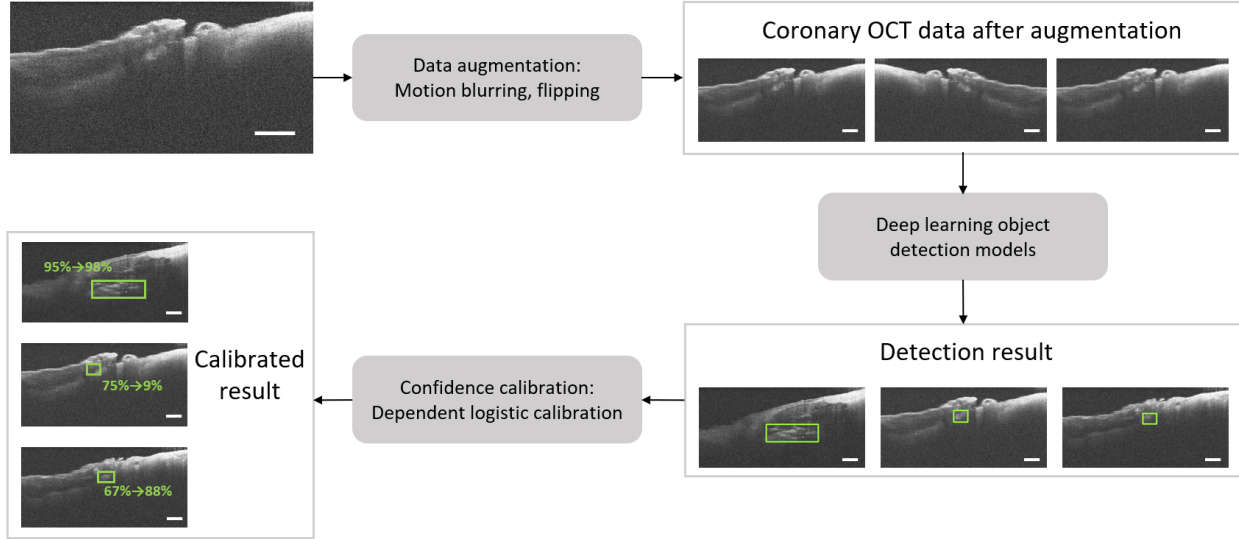


**Fig 1** Flowchart of the proposed work. Scale Bar:  $500\mu m$

## 2.2 Data augmentation

Various data augmentation techniques have been proposed to improve the performance of deep learning models.<sup>40</sup> In the time of imaging, the quality of OCT images may be impacted due to degradation caused by motion blur,<sup>41,42</sup> which appears when a camera is moving during image acquisition. A motion blur filter is used to simulate this effect of real-world conditions.<sup>43</sup> Other common augmentation strategies, such as flipping, cropping, scaling, Gaussian noise, rotation, and shears, are routinely performed.<sup>44</sup> Noticeably, we do not prefer vertical flipping and rotation in OCT images, because the light propagates in a fixed direction, applying such methods will change the nature of OCT images.

Therefore, in this work, two copies of each OCT image are created by applying a motion-blurring filter and flipping horizontally for training the deep learning model.

### 2.3 Object detection

Object detection creates bounding box regions that identify an object’s position, size, and class within an image. We opt to use You-Only-Look-Once v5 (YOLO)<sup>45</sup> to rapidly identify the bounding box and tissue types within an OCT image. Because of its lightweight and feature-reuse properties, YOLO architecture is powerful to realize fast and accurate detection. As the schematic shown in Fig. 2, YOLO enhances detection performance by utilizing different scales of feature maps to generate predictions for objects of different sizes.

The predictions have the outputs in two branches, confidence scores (*confidence*) and bounding boxes ( $x_{center}, y_{center}, width, height$ ). In the confidence score branch, the confidence score indicates a certain level that the prediction is true. In the bounding boxes branch, the values of the center coordinate, together with the width and height of the bounding box, depict the location of the predicted bounding box.

### 2.4 Uncertainty measurement and confidence calibration

The common use of calibration is for the classification task, where only the confidence score can be utilized for a given image. In object detection, one additional piece of information that can be included for calibration is the location and scale of the bounding box. Therefore, in the object detection task, the criterion of a calibrated model is defined as the precision of a prediction given the confidence, class category, and bounding box information,<sup>46</sup> as in Eq. 1:

$$P(\text{correct prediction} \mid p \hat{=} \text{confidence}, y \hat{=} y, r \hat{=} r) = \text{confidence}, \quad (1)$$
$$\forall \text{confidence} \in [0, 1], y \in Y, r \in [0, 1]^K$$

where  $y$  is the predicted class, and  $r$  is the bounding box information with  $k$  dimensions.

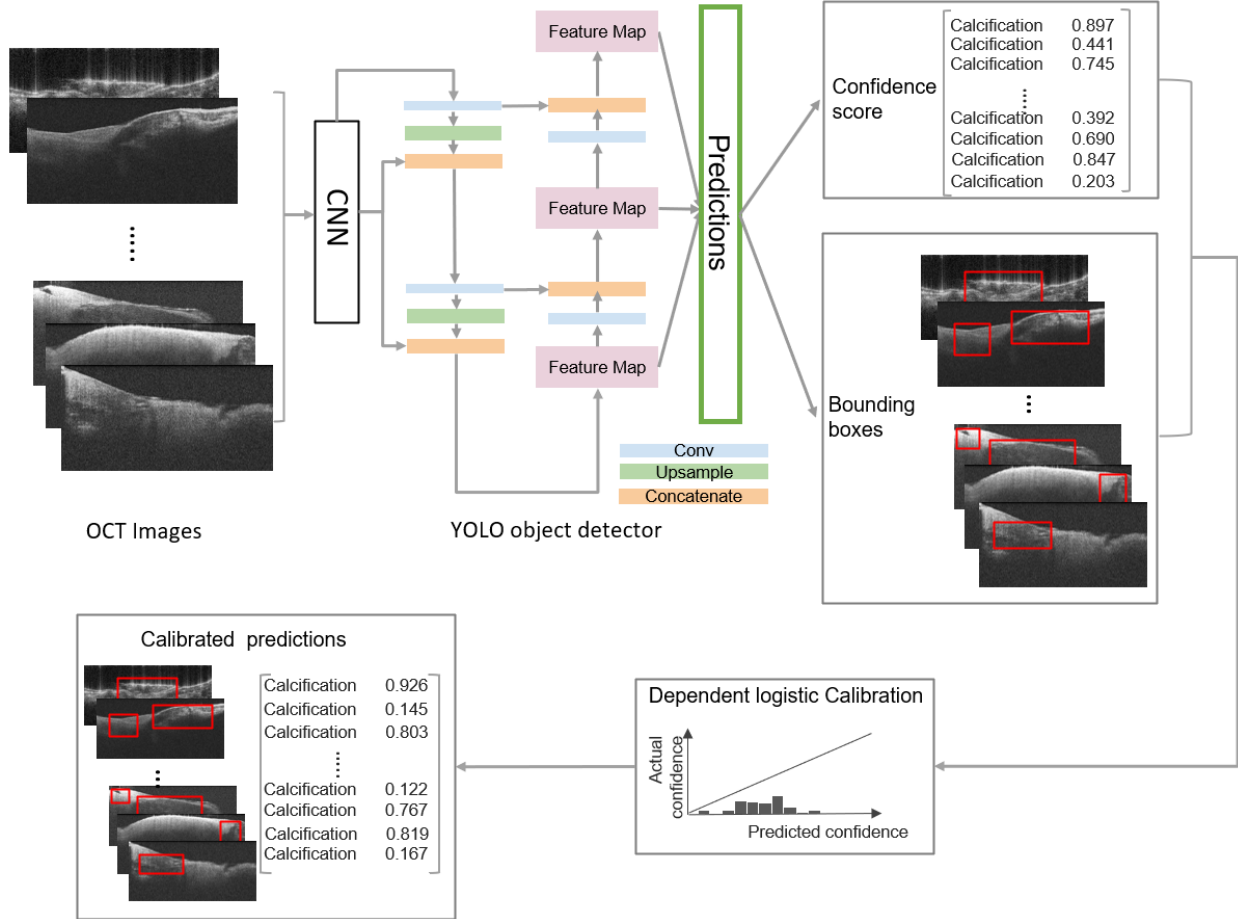


**Fig 2** The schematic of YOLO object detector and calibration.

Expected Calibration Error (ECE) is used to measure the uncertainty of the prediction of the deep learning model. The ECE of object detection is calculated by binning the confidence  $\hat{p}$  into  $M$  equally spaced bins. Samples with different confidence scores fall into corresponding bins.  $B_m$  is the number of samples in a bin. The *Precision* and *Confidence* are the average precision and average confidence respectively among the samples in a bin. The ECE is given by:

$$ECE = \sum_{m=1}^M \frac{|B_m|}{N} |Precision(m) - Confidence(m)| \quad (2)$$

For confidence calibration, in this work, we take two additional bounding box information, the



center-x and center-y position along with the confidence score to calibrate the prediction results using the dependent logistic calibration,<sup>46</sup> where the multivariate probability density function is used to model the log-likelihood ratio (lr) of the combined input(*confidence, bounding box*). Taking the correlations between confidence and the bounding box into consideration, the calibration map is defined as  $g$ :

$$g(input) \approx \frac{1}{1 + e^{-lr(input)}}, \quad lr(s) = \frac{1}{2}[(s_-^T \Sigma_-^{-1} s_-) - (s_+^T \Sigma_+^{-1} s_+)] + c \quad (3)$$

For the variable  $s$ ,  $s_+ = s - \mu_+$  and  $s_- = s - \mu_-$ , and  $c = \log \left| \frac{V_-}{V_+} \right|$ , with  $\mu_+$  and  $\mu_-$  as the mean vectors,  $\Sigma_-$  and  $\Sigma_+$  as the covariance matrices for incorrect and correct prediction respectively, for the true and false predictions. As shown in the calibrated predictions block in Fig. 2, a new confidence score for each prediction is obtained by mapping the input to the calibration map  $g$ . The ECE of the prediction results before and after calibration is calculated to test the effect of calibration on model uncertainty.

### 3 Results

#### 3.1 Experimental setup

For model development, we use 943 OCT images, from 14 OCT specimen segments, for a three-fold cross-validation. The OCT images were acquired from specimens that contain calcification regions, which include essential information for CAD treatments. Within each OCT volume, B-scans were sampled at an interval of 20. Each B-scan is with a size of  $1024 \times 1500$  pixels, corresponding to a space of  $1.98 \times 3 \text{ mm}^2$ . In the confidence calibration stage, 60% predictions are used to fit the calibration model, with the rest 40% predictions to be tested.

The YOLO was built in Python 3.8, PyTorch 1.10, CUDA 11.1, and NVIDIA RTX 6000, and a pre-trained weight<sup>47</sup> was used in this work, with batch size of 8, the learning rate of 0.001 using Adam optimizer. In addition to YOLO, another object detection scheme, Single Shot Multibox Detector (SSD),<sup>48</sup> was trained for comparison purposes. The SSD was built in Python 3.8, PyTorch 1.10, CUDA 11.1, and NVIDIA RTX 6000, the training process started by loading pre-trained weight,<sup>49</sup> with batch size of 8, the learning rate of 0.001 using stochastic gradient descent optimizer with the momentum of 0.9.

### 3.2 Object detection

To evaluate the performance of calcification detection, three metrics, precision, recall, and f1-score, are calculated, as given in Eq.(4 ~ 6).

$$Precision = \frac{\# \text{ of true positive}}{\# \text{ of true positive} + \# \text{ of false positive}} \quad (4)$$

$$Recall = \frac{\# \text{ of true positive}}{\# \text{ of true positive} + \# \text{ of false negative}} \quad (5)$$

$$f1 - score = \frac{2 \times precision \times recall}{precision + recall} \quad (6)$$

where the true positive means the model correctly predicts the region with calcification, the false negative is the wrong prediction for the region that has calcification, and the false positive is the wrong prediction for the region with no calcification. Precision indicates the number of correct predictions among all detection. Recall measures the fraction of correct predictions among ground

truths. The f1-score is a measure of overall model performance by combining precision and recall.

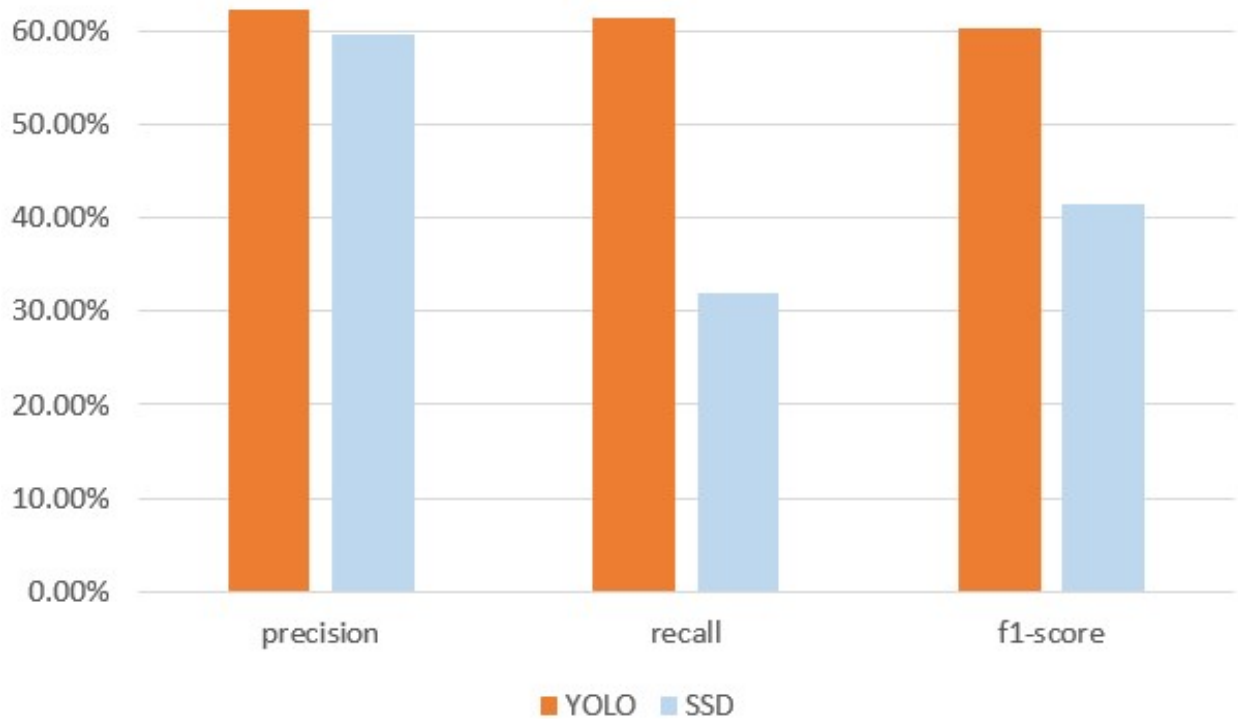


**Fig 3** Object detection results of deep learning models in precision, recall, and f-1 score. The green bars are the results of YOLO, and the blue bars are the results of SSD.

The quantitative results in Fig.3 indicate that YOLO generally outperforms SSD in detecting calcification in coronary OCT images. YOLO outperforms SSD by  $\sim 5\%$  in precision,  $\sim 30\%$  in recall, and  $\sim 19\%$  in f1-score. The lower recall of SSD reveals higher false negative predictions, which agrees with the observation in Fig. 4, where YOLO predicts all calcification in this coronary OCT image while SSD fails to detect the calcification region in relatively lower contrast.

Besides, as shown in table 1, the processing speed of YOLO is 140 frames per second (fps), while SSD processes at 68 fps, showing that YOLO has great capability for real-time detection, which is especially desirable in the circumstance of processing the large volume of OCT images. Comparatively, the runtime of OCT segmentation is approximately 15 fps,<sup>50,51</sup> which indicates a larger computational burden than detection.

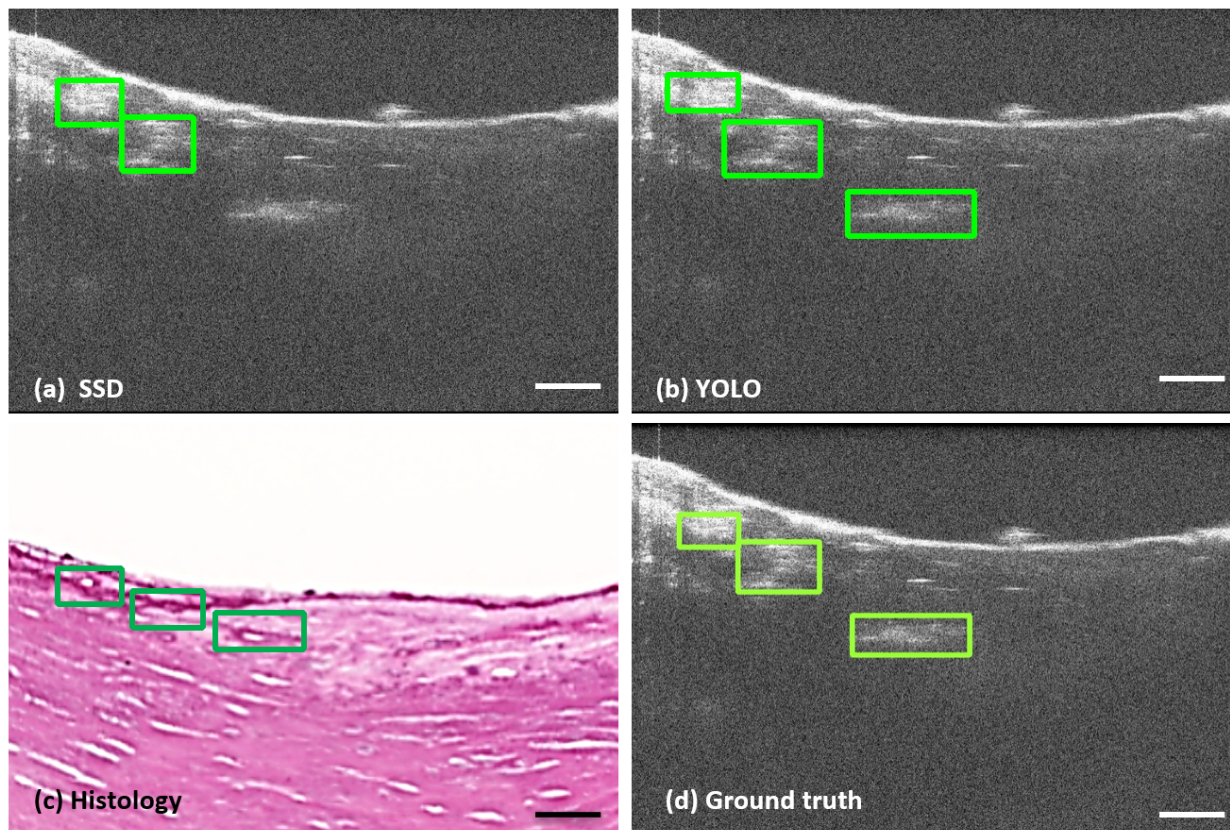


**Fig 4** Object detection results from (a) SSD, (b) YOLO. (c) corresponding histology, and (d) ground truth label. Scale Bar:  $500\mu m$

	YOLO	SSD
runtime (fps)	140	68

**Table 1** Runtime in frames per second (fps) for deep learning models detecting calcification in coronary OCT images in this work.

### 3.3 Uncertainty measurement and confidence calibration

We evaluate the effectiveness of the calibration of predictions from both deep learning models. In Fig. 5, the adjustment of confidence scores is observed in the calibrated predictions in YOLO and SSD. In Fig. 5a, the prediction from SSD in the red box gets the confidence score slightly adjusted from 91% to 88%. In Fig. 5b, the overconfident predictions shown in the yellow boxes reduced the confidence score from 46% to 18% after calibration, while the other confidence scores of predicted boxes are slightly adjusted.

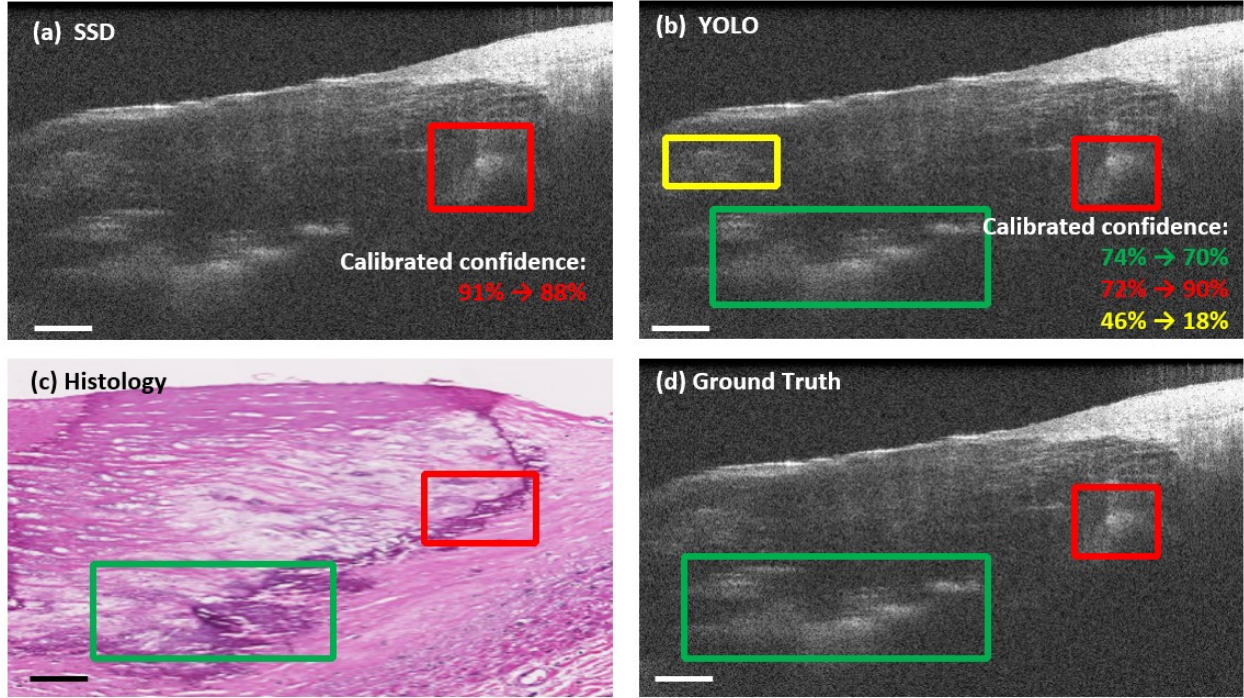


**Fig 5** Confidence calibration results of YOLO. (a) YOLO predictions, (b) ground truth labels, and (c) corresponding histology. Scale Bar:  $500\mu m$

	YOLO	SSD	Difference
ECE	0.233	0.731	0.498
Calibrated ECE	0.134	0.146	0.008
Before/After Calibration	0.099	0.585	—

**Table 2** The uncertainty measurements before and after confidence calibration: Expected Calibration Error (ECE), the last column shows the difference (SSD-YOLO) between two deep learning models. The rows of Before/After Calibration shows the changes in ECE during the calibration.

For quantitative evaluation, we use the ECE to measure the uncertainty of predictions. In Table 2, before calibration, YOLO has a lower level of uncertainty in ECE, indicating that YOLO produces more reliable predictions. For both YOLO and SSD, the calibration errors are lowered to the same level around  $\sim 0.14$  after implementing calibration, which proves that the calibration process can reduce the bias from different deep learning models and rectify the overconfident predictions of detectors.

## **4 Discussion and conclusion**

In this work, we report calcification detection in coronary OCT images using deep learning models with uncertainty measurements and confidence calibration to reduce the bias in deep learning models. Although tissue detection and segmentation in OCT images have been studied, to our best knowledge, this work is the first to implement uncertainty measurement and confidence calibration for deep learning-based calcification detection in coronary OCT images. We investigate and compare the calcification detection performance of YOLO with SSD, and prove that YOLO is superior to SSD in producing more accurate and reliable predictions by detection accuracy and uncertainty measures. With an exceptional runtime of 140 fps, YOLO has the potential to become the real-time detector for predicting calcification in coronary OCT images. This work also implements confidence calibration by integrating the bounding box information with the confidence score. The quantitative and qualitative results show the effectiveness of the calibration, indicating its practical value in safe-critical and risk-sensitive applications, for example, the calcification detection in coronary OCT images during PCI.

In the future, we will implement other calibration methods on the predicted confidence score and seek to ensemble multiple models in order to produce more robust and reliable predictions for calcification detection in OCT images. Furthermore, by providing additional information critical to diagnosis, the calibrated confidence and uncertainty measures can be used in future clinical practice.

### **Funding**

This work was supported in part by National Science Foundation (CRII-1948540), New Jersey Health Foundation, the National Center for Advancing Translational Research of the National

Institutes of Health underaward number UL1TR003096.

## **Disclosures**

All authors declare that they have no conflicts of interest.

## **Acknowledgements**

The authors would like to thank Dr. Dezhi Wang from the University of Alabama, Birmingham, for histology service.

## **Data availability statement**

The datasets generated and analyzed in this work are available from the corresponding author upon reasonable request.

## *References*

- 1 M. Nichols, N. Townsend, P. Scarborough, *et al.*, “Cardiovascular disease in europe: epidemiological update,” *European heart journal* **34**(39), 3028–3034 (2013).
- 2 A. S. Go, D. Mozaffarian, V. L. Roger, *et al.*, “Heart disease and stroke statistics—2014 update: a report from the american heart association,” *Circulation* **129**(3), e28–e292 (2014).
- 3 K. Okrainec, D. K. Banerjee, and M. J. Eisenberg, “Coronary artery disease in the developing world,” *American heart journal* **148**(1), 7–15 (2004).
- 4 I. Moussa, S. G. Ellis, M. Jones, *et al.*, “Impact of coronary culprit lesion calcium in patients undergoing paclitaxel-eluting stent implantation (a taxus-iv sub study),” *The American journal of cardiology* **96**(9), 1242–1247 (2005).

- 5 M. Farag, C. Costopoulos, D. A. Gorog, *et al.*, “Treatment of calcified coronary artery lesions,” *Expert review of cardiovascular therapy* **14**(6), 683–690 (2016).
- 6 R. Kawaguchi, H. Tsurugaya, H. Hoshizaki, *et al.*, “Impact of lesion calcification on clinical and angiographic outcome after sirolimus-eluting stent implantation in real-world patients,” *Cardiovascular Revascularization Medicine* **9**(1), 2–8 (2008).
- 7 L. K. Kim, D. N. Feldman, R. V. Swaminathan, *et al.*, “Rate of percutaneous coronary intervention for the management of acute coronary syndromes and stable coronary artery disease in the united states (2007 to 2011),” *The American Journal of Cardiology* **114**(7), 1003–1010 (2014).
- 8 F. Migliavacca, L. Petrini, M. Colombo, *et al.*, “Mechanical behavior of coronary stents investigated through the finite element method,” *Journal of biomechanics* **35**(6), 803–811 (2002).
- 9 V. Sinitsyn, M. Belkind, Y. Matchin, *et al.*, “Relationships between coronary calcification detected at electron beam computed tomography and percutaneous transluminal coronary angioplasty results in coronary artery disease patients,” *European radiology* **13**(1), 62–67 (2003).
- 10 Y. Gharaibeh, D. S. Prabhu, C. Kolluru, *et al.*, “Coronary calcification segmentation in intravascular oct images using deep learning: application to calcification scoring,” *Journal of Medical Imaging* **6**(4), 045002 (2019).
- 11 E. R. Edelman and C. Rogers, “Pathobiologic responses to stenting,” *The American journal of cardiology* **81**(7), 4E–6E (1998).
- 12 G. D. Dangas, B. E. Claessen, A. Caixeta, *et al.*, “In-stent restenosis in the drug-eluting stent era,” *Journal of the American College of Cardiology* **56**(23), 1897–1907 (2010).



- 13 K. Fujii, S. G. Carlier, G. S. Mintz, *et al.*, “Stent underexpansion and residual reference segment stenosis are related to stent thrombosis after sirolimus-eluting stent implantation: an intravascular ultrasound study,” *Journal of the American College of Cardiology* **45**(7), 995–998 (2005).
- 14 G. F. Attizzani, D. Capodanno, Y. Ohno, *et al.*, “Mechanisms, pathophysiology, and clinical aspects of incomplete stent apposition,” *Journal of the American College of Cardiology* **63**(14), 1355–1367 (2014).
- 15 H. Doi, A. Maehara, G. S. Mintz, *et al.*, “Impact of post-intervention minimal stent area on 9-month follow-up patency of paclitaxel-eluting stents: an integrated intravascular ultrasound analysis from the taxus iv, v, and vi and taxus atlas workhorse, long lesion, and direct stent trials,” *JACC: Cardiovascular Interventions* **2**(12), 1269–1275 (2009).
- 16 M.-K. Hong, G. S. Mintz, C. W. Lee, *et al.*, “Intravascular ultrasound predictors of angiographic restenosis after sirolimus-eluting stent implantation,” *European heart journal* **27**(11), 1305–1310 (2006).
- 17 N. G. Uren, S. Schwarzacher, J. Metz, *et al.*, “Predictors and outcomes of stent thrombosis. an intravascular ultrasound registry,” *European heart journal* **23**(2), 124–132 (2002).
- 18 S. Mehrotra, S. Mishra, and G. Paramasivam, “Imaging during percutaneous coronary intervention for optimizing outcomes,” *Indian heart journal* **70**, S456–S465 (2018).
- 19 G. Richards and T. Johnson, “A vision of percutaneous coronary revascularisation in 2021: How to take advantage of intra-coronary imaging to perform more effective pci,” *JRSM Cardiovascular Disease* **10**, 20480040211049978 (2021).
- 20 A. Fujino, G. S. Mintz, M. Matsumura, *et al.*, “A new optical coherence tomography-based

- calcium scoring system to predict stent underexpansion.,” *EuroIntervention: journal of EuroPCR in collaboration with the Working Group on Interventional Cardiology of the European Society of Cardiology* **13**(18), e2182–e2189 (2018).
- 21 F. Prati, G. Guagliumi, G. S. Mintz, *et al.*, “Expert review document part 2: methodology, terminology and clinical applications of optical coherence tomography for the assessment of interventional procedures,” *European heart journal* **33**(20), 2513–2520 (2012).
- 22 H. G. Bezerra, M. A. Costa, G. Guagliumi, *et al.*, “Intracoronary optical coherence tomography: a comprehensive review: clinical and research applications,” *JACC: Cardiovascular Interventions* **2**(11), 1035–1046 (2009).
- 23 W. Wu, J. Zhang, H. Xie, *et al.*, “Automatic detection of coronary artery stenosis by convolutional neural network with temporal constraint,” *Computers in biology and medicine* **118**, 103657 (2020).
- 24 Y. Tong, W. Lu, Y. Yu, *et al.*, “Application of machine learning in ophthalmic imaging modalities,” *Eye and Vision* **7**(1), 1–15 (2020).
- 25 L. S. Athanasiou, M. L. Olender, M. José, *et al.*, “A deep learning approach to classify atherosclerosis using intracoronary optical coherence tomography,” in *Medical Imaging 2019: Computer-Aided Diagnosis*, **10950**, 163–170, SPIE (2019).
- 26 A. Abdolmanafi, L. Duong, N. Dahdah, *et al.*, “Characterization of coronary artery pathological formations from oct imaging using deep learning,” *Biomedical optics express* **9**(10), 4936–4960 (2018).
- 27 J. Lee, Y. Gharaibeh, C. Kolluru, *et al.*, “Segmentation of coronary calcified plaque in in-

- travascular oct images using a two-step deep learning approach,” *IEEE Access* **8**, 225581–225593 (2020).
- 28 Y. Avital, A. Madar, S. Arnon, *et al.*, “Identification of coronary calcifications in optical coherence tomography imaging using deep learning,” *Scientific Reports* **11**(1), 1–7 (2021).
- 29 H. Shibutani, K. Fujii, D. Ueda, *et al.*, “Automated classification of coronary atherosclerotic plaque in optical frequency domain imaging based on deep learning,” *Atherosclerosis* **328**, 100–105 (2021).
- 30 J. Lee, D. Prabhu, C. Kolluru, *et al.*, “Automated plaque characterization using deep learning on coronary intravascular optical coherence tomographic images,” *Biomedical Optics Express* **10**(12), 6497–6515 (2019).
- 31 H. Sun, C. Zhao, Y. Qin, *et al.*, “In vivo detection of plaque erosion by intravascular optical coherence tomography using artificial intelligence,” *Biomed. Opt. Express* **13**, 3922–3938 (2022).
- 32 B. Ghoshal and A. Tucker, “On calibrated model uncertainty in deep learning,” *arXiv preprint arXiv:2206.07795* (2022).
- 33 J. Platt *et al.*, “Probabilistic outputs for support vector machines and comparisons to regularized likelihood methods,” *Advances in large margin classifiers* **10**(3), 61–74 (1999).
- 34 B. Zadrozny and C. Elkan, “Obtaining calibrated probability estimates from decision trees and naive bayesian classifiers,” in *Icml*, **1**, 609–616, Citeseer (2001).
- 35 C. Guo, G. Pleiss, Y. Sun, *et al.*, “On calibration of modern neural networks,” in *International conference on machine learning*, 1321–1330, PMLR (2017).

- 36 L. Tran, B. S. Veeling, K. Roth, *et al.*, “Hydra: Preserving ensemble diversity for model distillation,” *arXiv preprint arXiv:2001.04694* (2020).
- 37 Y. Wen, D. Tran, and J. Ba, “Batchensemble: an alternative approach to efficient ensemble and lifelong learning,” *arXiv preprint arXiv:2002.06715* (2020).
- 38 S. Cao, X. Yao, N. Koirala, *et al.*, “Super-resolution technology to simultaneously improve optical & digital resolution of optical coherence tomography via deep learning,” in *2020 42nd Annu. Int. Conf. IEEE Eng. Med. Biol. Soc.*, 1879–1882, IEEE (2020).
- 39 X. Li, S. Cao, H. Liu, *et al.*, “Multi-scale reconstruction of undersampled spectral-spatial oct data for coronary imaging using deep learning,” *IEEE Transactions on Biomedical Engineering* (2022).
- 40 Z. Hussain, F. Gimenez, D. Yi, *et al.*, “Differential data augmentation techniques for medical imaging classification tasks,” in *AMIA annual symposium proceedings*, **2017**, 979, American Medical Informatics Association (2017).
- 41 M. F. Kraus, B. Potsaid, M. A. Mayer, *et al.*, “Motion correction in optical coherence tomography volumes on a per a-scan basis using orthogonal scan patterns,” *Biomedical optics express* **3**(6), 1182–1199 (2012).
- 42 J. Lian, S. Hou, X. Sui, *et al.*, “Deblurring retinal optical coherence tomography via a convolutional neural network with anisotropic and double convolution layer,” *IET Computer Vision* **12**(6), 900–907 (2018).
- 43 O. O. Abayomi-Alli, R. Damaševičius, S. Misra, *et al.*, “Cassava disease recognition from low-quality images using enhanced data augmentation model and deep learning,” *Expert Systems* **38**(7), e12746 (2021).

- 44 A. Sharif Razavian, H. Azizpour, J. Sullivan, *et al.*, “CNN features off-the-shelf: an astounding baseline for recognition,” in *Proceedings of the IEEE conference on computer vision and pattern recognition workshops*, 806–813 (2014).
- 45 G. Jocher, A. Stoken, J. Borovec, *et al.*, “ultralytics/yolov5: v3.1 - Bug Fixes and Performance Improvements,” (2020).
- 46 F. Kuppers, J. Kronenberger, A. Shantia, *et al.*, “Multivariate confidence calibration for object detection,” in *Proceedings of the IEEE/CVF Conference on Computer Vision and Pattern Recognition Workshops*, 326–327 (2020).
- 47 glenn jocher, “Yolo5s pre-trained weight using coco dataset,” (2021).
- 48 W. Liu, D. Anguelov, D. Erhan, *et al.*, “Ssd: Single shot multibox detector,” in *European conference on computer vision*, 21–37, Springer (2016).
- 49 Tensorflow, “Ssd mobilenet v2 pretrained weight using coco2017 dataset,” (2021).
- 50 Y. He, A. Carass, B. M. Jedynek, *et al.*, “Topology guaranteed segmentation of the human retina from oct using convolutional neural networks,” *arXiv preprint arXiv:1803.05120* (2018).
- 51 A. Shah, L. Zhou, M. D. Abrámoff, *et al.*, “Multiple surface segmentation using convolution neural nets: application to retinal layer segmentation in oct images,” *Biomedical optics express* **9**(9), 4509–4526 (2018).

**Hongshan Liu** received her M.S. degree in Electrical Engineering from University of Michigan-Ann Arbor and her B.S. degree in Physics from Zhejiang University. She is a doctoral student in Biomedical Engineering at Stevens Institute of Technology. Her research focuses on deep learning-based image processing in the clinical applications of optical coherence tomography.

**Xueshen Li** received his M.S. degree in Biomedical Engineering from Eindhoven University of Technology. He is a doctoral student in Biomedical Engineering department at Stevens Institute of Technology. His research focuses on biomedical image processing.

**Abdul Latif Bamba** is an undergraduate student from Columbia University. His research is in image processing, microelectronic and solid-state devices.

**Xiaoyu Song** received her DrPH in Biostatistics from Columbia University. She is an Assistant Professor at the Icahn School of Medicine at Mount Sinai. Her research interest is in biostatistics and statistical genomics.

**Brigitta C. Brott, MD** is an interventional cardiologist with a background in Materials Science and Engineering. She obtained her cardiology and interventional cardiology training at Duke University Medical Center. She is a Professor of Medicine and Biomedical Engineering at the University of Alabama at Birmingham. Her research interests include novel coatings to improve healing after device implantation, and optimization of imaging and physiology assessments to guide cardiac interventional procedures.

**Silvio H. Litovsky** received his MD degree from the University of Buenos Aires, Argentina. He is Professor of Pathology at the University of Alabama at Birmingham. His research interest includes multiple areas of cardiovascular pathology including high risk atherosclerotic plaques.

**Yu Gan** received his PhD degree in Electrical Engineering from Columbia University. He is an Assistant Professor in Biomedical Engineering at Stevens Institute of Technology. His research interest is in optical coherence tomography, biomedical image processing, and computer vision.